All Optical Fiber Optofluidic or Ferrofluidic Microsensors Fabricated by Femtosecond Laser Micromachining

60

Hai Xiao, Lei Yuan, Baokai Cheng, and Yang Song

Contents

Abstract

Research and development in photonic micro-/nanostructures functioned as sensors have experienced significant growth in recent years, fueled by their broad applications in the fields of physical, chemical, and biological quantities. Compared with conventional sensors with bulky assemblies, recent progress

H. Xiao (✉) · L. Yuan · B. Cheng · Y. Song
Department of Electrical and Computer Engineering, Center for Optical Materials Science and Engineering Technologies (COMSET), Clemson University, Clemson, SC, USA
e-mail: haix@clemson.edu; yuan7@clemson.edu; baokaic@g.clemson.edu; song5@g.clemson.edu

G.-D. Peng (ed.), *Handbook of Optical Fibers*,
https://doi.org/10.1007/978-981-10-7087-7_63

in femtosecond (fs) laser three-dimensional (3D) micromachining technique has been proven an effective way for one-step fabrication of assembly-free microstructures in various transparent materials (i.e., fused silica). When used for fabrication, fs laser has many unique characteristics, such as negligible cracks, minimal heat-affected zone, low recast, high precision, and the capability of embedded 3D fabrication, compared with conventional long pulse lasers (i.e., ns laser). The merits of this advanced manufacturing technique enable the unique opportunity to fabricate integrated sensors with improved robustness, enriched functionality, enhanced intelligence, and unprecedented performance.

Recently, fiber-optic sensors have been widely used in many application areas, such as aeronautics and astronautics, petrochemical industry, chemical detection, biomedical science, homeland security, etc. In addition to the well-known advantages of miniaturized in size, high sensitivity, immunity to electromagnetic interference (EMI), and resistance to corrosion, fiber-optic sensors are becoming more and more desirable when designed with characteristics of assembly-free and operation in the reflection configuration. Additionally, such sensors are also needed in optofluidic/ferrofluidic systems for chemical/biomedical sensing applications.

In this chapter, liquid-assisted laser micromachining techniques were investigated for the fabrication of assembly-free, all-optical fiber sensor probes. All-in-fiber optofluidic sensor and fiber in-line ferrofluidic sensor were presented as examples with respect to these laser processing techniques.

Introduction

The invention of the ruby laser in 1960 (Maiman 1960) provided much higher laser intensities than previous candidates. Since then, laser has been developed rapidly and used for controllable material processing by high laser intensities. With the advances of mode-locking techniques (Spence et al. 1991) and chirped pulse amplification (Strickland and Mourou 1985), the intensities of commercially available femtosecond (fs) laser systems can be achieved of more than 10^{13} W/cm^2 (Perry and Mourou 1994). At such intensities, any materials, especially for transparent materials, will be ionized and exhibit nonlinear behavior, causing dielectric breakdown and structural change in transparent materials (Itoh et al. 2006).

Fs laser is also known as ultrafast laser, due to its unique advantages of ultrashort pulse width (<200fs, 1fs $= 10^{-15}$s) and extremely high peak intensity (>10^{15} W/cm^2). Recently, fs laser micromachining has opened up a new avenue for material processing, especially for the transparent materials with large material bandgaps (i.e., fused silica (Eg $= 9$ eV)). When used for fabrication, fs laser can be used either to remove materials from the surface (ablation) or to modify the properties inside the materials (modification or irradiation). Compared with long pulse lasers (pulses longer than a few picoseconds) (Chichkov et al. 1996), fs laser has many unique characteristics, such as negligible cracks, minimal heat-affected zone, low recast, and high precision.

Initial studies of fs laser micromachining were first demonstrated in 1987, when ultrafast excimer UV lasers were used to ablate the surface of polymethyl methacrylate (PMMA) (Du et al. 1994). Later, micrometer-sized features on silica (Pronko et al. 1995) and silver surfaces (Chimmalgi et al. 2003) were performed using infrared fs laser systems. In less than 10 years, the resolution of surface ablation has improved to enable high precision with nanometer scale (Küper and Stuke 1987). For the material modification, Hirao's group firstly demonstrated fs laser processed in the bulk of transparent glass in 1996, and the material modification happened beneath the sample surface, forming waveguiding structures with a permanent refractive index change localized to the focal volume (Davis et al. 1996). This was followed by introducing two-photon polymerization into a resin (Kawata et al. 2001) and printing complex three-dimensional (3D) structures with nanometer-scale resolution. Over the past decade, fs laser micromachining has been used in a broad range of applications, from waveguide writing, cell ablation to biological sample modification (Gattass and Mazur 2008). As a result, fs laser was proven to be a unique and versatile contactless material modification tool.

The fiber-optic field has undergone tremendous growth and advancement over the past 50 years. Initially considered as a medium of transmitting light and imagery for medical endoscopic applications, optical fibers were later promoted as an information carrier for telecommunication applications in the mid-1960s (Bates 2001). C. Kao and G. Hockham of the British company Standard Telephones and Cables (STC) were the first to propose the idea that the attenuation in optical fibers could be controlled down to 20 dB/km, allowing fibers to be a good candidate for telecommunication applications (Hecht 2004). Since then, the research and development of optical fiber telecommunication applications have been widened immensely (Udd 1995). Today, optical telecommunication has proven to be the preferred method to transmit vast amounts of data and information with high speed and long-haul capability.

In addition to communication applications, optical fibers have been widely used for broad sensing applications in the fields of physical, chemical, and biological analyses, including structure health monitoring, harsh environment temperature sensing, biological and chemical refractive index/pH sensors, and medical imaging (Haque et al. 2014; Liu et al. 2013; Wei et al. 2008; Zhang et al. 2013; Zhou et al. 2010). Optical fiber, most of the time, is made of fused silica glass. It consists of fiber core, fiber cladding, and the outside buffer/jacket layer for protection, as shown in Fig. 1. Due to the small amount of doping elements (i.e., germanium-doped) in the fiber core area, the refractive index of fiber core (n_1) is slightly larger than the index of fiber cladding (n_2), so the light can propagate inside the fiber core due to the so-called total internal reflection (TIR). Compared with electrical sensors, fiber-optic sensors offer many intrinsic advantages, such as small size/lightweight, immunity to electromagnetic interference (EMI), resistance to chemical corrosion, high temperature capability, high sensitivity, and multiplexing and distributed sensing.

Fiber-optic sensors have been long envisioned as a cost-effective and reliable candidate for many applications. However, although the past half century has seen a

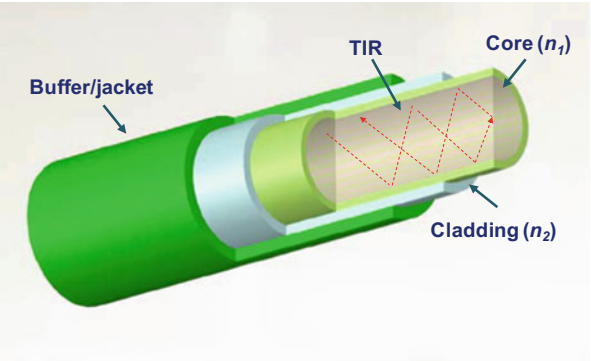

Fig. 1 Schematic representation of the optical fiber as a waveguide under TIR conditions

steady growth of appearance of optical fibers in various industry sectors, the market of fiber-optic sensors has not blew out as expected. On the contrary, many of the unique advantages and special requirements of advanced fiber-optic sensors and devices are yet to be fully harvested, including assembly-free, inexpensive, and miniaturized fiber-pigtailed sensor probes as well as long-haul, fully distributed fiber-optic sensor networks.

Special requirements for advanced fiber-optic sensors are highly needed in biomedical/chemical applications, i.e., the hot topic of optofluidic systems. Aiming to synergistically combine integrated optics and microfluidics, optofluidic-based systems have attracted much research interest because of their unique advantages toward biological/chemical sensing applications (Fan and White 2011). In an optofluidic system, the liquid of interest is constrained and manipulated in a small geometry to interact with the optics. As such, the physical, chemical, and biological properties of the liquid can be probed and analyzed effectively using optical means (Psaltis et al. 2006).

Most optofluidic systems have been constructed on a planar platform with microchannels in silica/polymetric materials and probed by a variety of optical means, such as absorbance, fluorescence, refractometry, Raman scattering, etc. (Monat et al. 2007). Objective lenses are commonly used to couple light into and out of the microfluidics (Woolley and Mathies 1994). However, the need of using a microscope to perform the optical alignment limits its field applicability. A number of efforts have been made to fabricate optical waveguides inside the substrate to confine and transport light in the substrate (Osellame et al. 2007) or directly integrate optical fibers with the fluidics for excitation and probing (Domachuk et al. 2006). However, the transmission efficiency of light coupling is still a challenge in most optofluidic configurations.

In addition to planar configurations, it has been suggested that the microfluidics can be directly fabricated on an optical fiber to form the so-called all-in-fiber optofluidics. The all-in-fiber configuration has the unique advantage of alignment-free optics and improved robustness. Examples include the photonic crystal fibers (PCFs) filled with functional fluids in their cladding air voids (Jensen et al.

2004), the capillary-based optofluidic ring resonator (OFRR) with a microchannel for sample delivery (Zhu et al. 2008), and a miniaturized microchannel directly fabricated on a conventional optical fiber for light-fluid interaction (Lai et al. 2006). While the PCF-based and OFRR-based optofluidic sensors utilize the evanescent fields to probe the fluid, the microchannel on a conventional fiber configuration allows a direct light passage through the liquid.

However, PCFs are still expensive, and huge transmission loss will be generated when fusion splicing PCFs with single-mode fibers (SMFs). OFRR structure needs to assemble with an ultrathin and fragile fiber-optic taper to read out the signal, limiting the application within the lab condition. Although the sensor with a microchannel in an SMF can probe the liquid, the sensing mechanism is still based on the intensity modulation, whose sensitivity and detection limit are much smaller and higher, respectively, than those of phase modulation-based sensors.

Similar to optofluidic systems, filling the embedded microchannels with functional liquids (i.e., ferrofluid) can also allow people to test surrounding magnetic field. Typically, varying magnetic field can change the properties of ferrofluid (i.e., the permittivity of the liquid) and then make the integrated device function as a ferrofluidic sensor for various applications. Additionally, it's highly desired that the ferrofluidic sensor can be directly implemented in an all-fiber form with minimum insertion loss and desired performance.

In this chapter, first of all, a brief overview of the background physics describing fs laser micromachining of transparent materials was presented. The discussion of laser/matter interactions was starting from atomic scale-free electron plasma formation to energy deposition and material modification. Secondly, the development of a typical home-integrated fs laser micromachining system and preliminary fabrication results were presented in details. After that, methods of liquid-assisted laser processing were illustrated. Buried microfluidic microchannels with sub-microresolution in an SMF can be fabricated either using laser-induced water breakdown technique directly or utilizing laser irradiation followed by chemical etching technique, resulting in fiber sensors for chemical/biomedical sensing application. Finally, an all-in-fiber optofluidic sensor and a fiber in-line ferrofluidic sensor are presented as examples of this technology.

Femtosecond Laser and Material Interactions

Free Electron Plasma Formation

The most popular femtosecond laser nowadays is Ti:sapphire laser which has its operating wavelength at around 800 nm. High-intensity focused fs laser pulses with the wavelength (λ) of 800 nm have insufficient photon energy ($E = h\nu = \hbar\omega = 1.55\text{eV}$, where $\omega = 2\pi\nu$) to be linearly absorbed in fused silica with the bandgap of material Eg, which is about 9 eV. As such, nonlinear photoionization is dominant to promote electrons from valence band to the conduction band and then generate free electrons. Typically, there are two classes of such

ionization process: nonlinear photoionization and avalanche ionization (Beresna et al. 2014). Nonlinear photoionization refers to direct electron excitation by an electric laser field. Such process can generate seed electrons that will participate in the next process. Photoionization involves multiphoton ionization and/or tunneling ionization depending on the laser frequency and intensity (Stuart et al. 1995). Once the free electrons exist in the conduction band, free carrier absorption happens, leading to collisional ionization followed by avalanche ionization.

In the multiphoton absorption regime, photoionization rate dn_e/dt strongly depends on the laser intensity:

$$\frac{dn_e(t,r,z)}{dt} = \delta_m (I(t,r,z))^m \tag{1}$$

where t is the time; r, the distance to the Gaussian beam axis; z, the depth from the surface of the bulk material; n_e is free electron density; $I(t, r, z)$ is the laser intensity inside the bulk material; m is the order of the multiphoton process, i.e., the number of photons should be six in our case to satisfy the condition $E = m\hbar\omega \geq E_g$; and δ_m is the cross section of the m-photon absorption. The tunnelling rate, on the other hand, scales more weakly with the laser intensity than the multiphoton rate (Schaffer et al. 2001).

The strong dependence on the intensity also means that the photoionization process is more efficient for the laser with short pulse duration. For the long pulse laser (i.e., ns), the photoionization process cannot efficiently generate sufficient seed electrons, and the excitation process becomes strongly reliant on the low concentration of impurities with energy levels which are distributed randomly close to the conduction band. As such, the modification process becomes less deterministic, and precise machining is impossible for longer pulses (Beresna et al. 2014).

Avalanche ionization involves free carrier absorption followed by impact ionization. The free electrons in the conduction band oscillate in the electromagnetic field of the laser and gradually gain energy by collisions. After the conduction band electron's energy exceeds the minimum energy of the conduction band by more than the bandgap energy of the material, it can impact ionize another bound electron from the valence band via collision, resulting in two excited electrons near the bottom of the conduction band (Yablonovitch and Bloembergen 1972). Both electrons can undergo free carrier absorption, impact ionization, and repeat the described energy transfer cycle. Such process will not stop until the laser electric field is dissipated and not strong enough, leading to an electronic avalanche. The density of free electrons generated through the avalanche ionization is:

$$\frac{dn_e(t,r,z)}{dt} = a_i I(t,r,z)\, n_e(t,r,z) \tag{2}$$

where a_i is the avalanche ionization coefficient (Stuart et al. 1996). The original laser beam before it interacts with the material is assumed to be a Gaussian distribution

in time and space. Obviously, at $z = 0$, it is assumed that the laser focus point is at the surface of the material.

The optical properties of the highly ionized dielectrics under an fs pulse can be well determined by plasma properties (Rethfeld et al. 2002). Generally, the plasma frequency ω_p is defined by (Mao et al. 2004):

$$\omega_p\left(n_e\right) = \sqrt{\frac{e^2 n_e(t)}{\varepsilon_0 m_e}} \tag{3}$$

where n_e is also denoted as free carrier density. When the free electron density excited by photoionization approaches a high density (i.e., $\omega_p \sim \omega \sim 10^{21}$ cm^{-3}), a large fraction of the remaining fs laser pulse can be absorbed (Schaffer et al. 2001). Assumed 800 nm laser irradiation, the plasma frequency ω_p equals the laser frequency ω when the free carrier density n_e is approximately 1.7×10^{21} cm^{-3}, which is also known as the critical density of free electrons ($n_c(t) = \omega^2 \varepsilon_0 m_e / e^2$). Such critical value can be also used as a criterion in the model of laser-material interaction.

It should be noticed that avalanche ionization requires the presence of seed electrons, which can trigger the process and is more efficient with longer pulse durations. The following rate equation has been widely used to describe this nonlinear photoionization process (the combined action of multiphoton excitation and avalanche ionization) (Stuart et al. 1996):

$$\frac{d n_e\left(t, r, z\right)}{d t} = \delta_m (I\left(t, r, z\right))^m + a_i I\left(t, r, z\right) n_e\left(t, r, z\right) \tag{4}$$

However, free carrier losses (i.e., self-trapping and recombination) may occur on a time scale comparable to pulse duration (<40 fs) of fs laser beam in large bandgap materials, such as quartz and fused silica. As such, the rate equation shown above should be modified (Schaffer et al. 2001). For longer pulse duration that is more than 150 fs, such losses can be neglected.

For material with defects or some dopants, initial electrons can be excited from these low-lying levels via linear absorption or thermal excitation (Schaffer et al. 2001). For pure dielectrics, such electrons are generated by nonlinear photoionization (i.e., ultrashort pulses). Then, free electron plasma formation is realized.

To summarize, for ultrafast laser pulses (i.e., sub-picosecond or even smaller), photon-electron interaction occurs on a faster time scale than energy transfer from hot free electrons to the lattice, separating the absorption and lattice heating processes (Schaffer et al. 2001). The plasma will become strongly absorbing when the density of free electrons in the conduction band increases through avalanche ionization until $\omega_p \approx \omega$. In another word, it's generally assumed that material modification/optical breakdown occurs at this critical point. In fused silica, the laser intensity needs to be $\sim 10^{13}$ W/cm^2 (Schaffer et al. 2001) to achieve optical breakdown.

Energy Deposition and Material Modification

When the absorbed laser energy, via free electron plasma formation process, is high enough, it can be transferred to the lattice (phonon) and then deposited into the material via electron-phonon coupling, equalizing the temperature of the free electrons and the lattice, resulting in the permanent material modification subsequently. Since the lattice heating time is on the order of 10 ps, which is much longer than the pulse duration of the fs laser beam, less energy is needed to achieve the intensity for optical breakdown with respect to short pulses, and high-precision micromachining can be realized (Gattass and Mazur 2008).

Although the free electron plasma created by absorbing fs laser pulses for nonlinear photoionization in transparent materials is widely accepted, the physical mechanisms for material modification are not fully understood. Davis and coworkers (Davis et al. 1996) first observed morphology changes and then generally classified into three types of structural formations: an isotropic refractive index formation (i.e., waveguide) (Davis et al. 1996), a nanograting formation (Sudrie et al. 1999), and a confined microexplosion and void formation (Glezer and Mazur 1997). In fused silica, these three morphologies can be observed by adjusting the pulse energy of the incident fs laser beam (Itoh et al. 2006), as shown in Fig. 2.

It should be noted that the permanent formations in transparent materials with large bandgap energy also depend on many other exposure parameters, such as

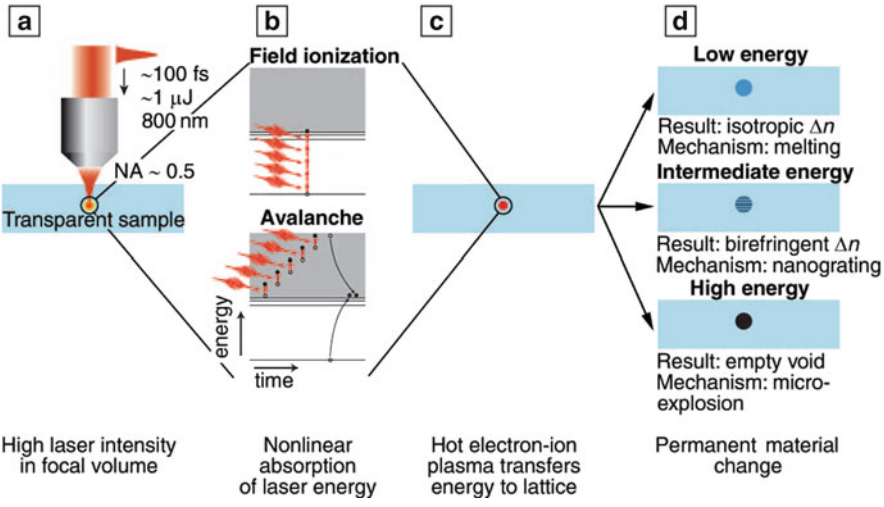

Fig. 2 Schematic illustration of physical mechanisms of intense fs laser pulses in transparent materials. (**a**) The laser is focused inside the sample leading to high laser intensity in focal volume. (**b**) The photon energy is nonlinearly absorbed, and the free electron plasma is generated by nonlinear photoionization. (**c**) The energy is transferred from hot electrons to lattice on a ~10 ps time scale. (**d**) Three types of permanent material modification, including isotropic refractive index change at low pulse energy, birefringent nanograting formation at intermediate energy, and empty void formation at high pulse energy (Itoh et al. 2006)

pulse duration, repetition rate, laser wavelength, polarization state, tight/loose focusing condition, as well as the scanning speed of the translation stage. Further explanations of mechanisms will be found in the following discussions.

If the laser beam is focusing on the surface of the transparent materials, the basic processes during laser ablation such as excitation, melting, and material removal are temporally separated when fs laser pulses are applied, allowing a separate investigation in different time scales. Once free electron and free carrier excitations are finished, several mechanisms can be involved that may give rise to damage or optical breakdown of a non-defect transparent material under fs laser excitation. It's widely accepted that thermal phase change includes melting and vaporization of the solid, following strong phonon emission induced by free electron plasma formation (Mao et al. 2004). For the physical mechanisms of nonthermal phase change, Coulomb explosion was proposed to explain single-shot ablation by fs laser pulses (Stoian et al. 2000). All the phase changes are highly depending on the material properties (i.e., bandgap Eg) and applied laser parameters (i.e., pulse duration τ_p and intensity I).

For laser pulses shorter than a few picoseconds, a substantial amount of energy will be transferred to the lattice during pulse propagation (Schaffer et al. 2001). The excited lattice phonons are diffusing thermal energy to the vicinity of the laser focal volume and then melting and causing permanent damage (depending on the critical plasma concentration) to the transparent material. These regimes and the time scales of the corresponding processes (Rethfeld et al. 2004) are shown in Fig. 3. For pulse

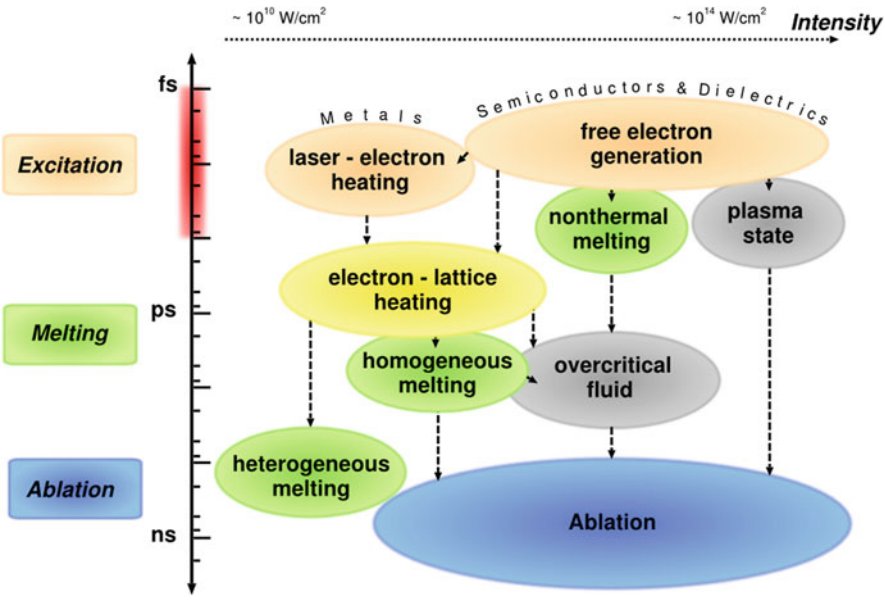

Fig. 3 Typical time scales versus intensity ranges of the phase changes occurring during and after irradiation of a solid with an fs laser pulse of about 100 fs duration. Excitation, melting, and ablation take place in the range of fs, ps, and ns regime, respectively (Rethfeld et al. 2004)

duration <10 ps, thermal diffusion and electron-ion interaction take place after the laser pulse; thus, the electrons can reach high temperatures, while keeping the lattice in the cold state during laser pulse irradiation, which is also called cold ablation. Such ablation mechanisms can make fs lasers an ideal tool to produce deterministic optical breakdown and damage near threshold and controllable material removal.

Our discussion of the structural changes induced by fs laser pulses on the surface or in the bulk of a transparent material was mainly based on single pulse interaction. However, when it comes to the multi-pulse condition within the same laser spot, the repetition rate may play a significant role during the structure formation. In general, two different modification regimes can be classified, including nonthermal and thermal regime (Gross and Withford 2015) (Fig. 4). If the repetition rate is low enough (i.e., 1 kHz), the generated heat in fused silica can be diffused out of the focal volume before the next pulse arrives. Typically, the thermal diffusion time in glass is ~1 μs (Carslaw and Jaeger 1959), which is much shorter than the time between two consecutive pulses (~1 ms). In this situation, structure is modified pulse-by-pulse without heat accumulation effect. Furthermore, in order to create a smooth waveguide inside the transparent material, pulses need to be spatially overlapped, which may limit the translation speed and increase the fabrication time.

For high repetition rates from hundreds of kHz to several MHz regimes, the time between laser pulses is less than the heat diffusion time in transparent material, resulting in cumulative heating in the focal volume (Schaffer et al. 2003). Thus, the material within the focal volume will be locally melted, and the melted volume increases in size, until the laser is removed. After rapid cooling, the modified structure is formed with altered refractive index change. For a waveguide structure,

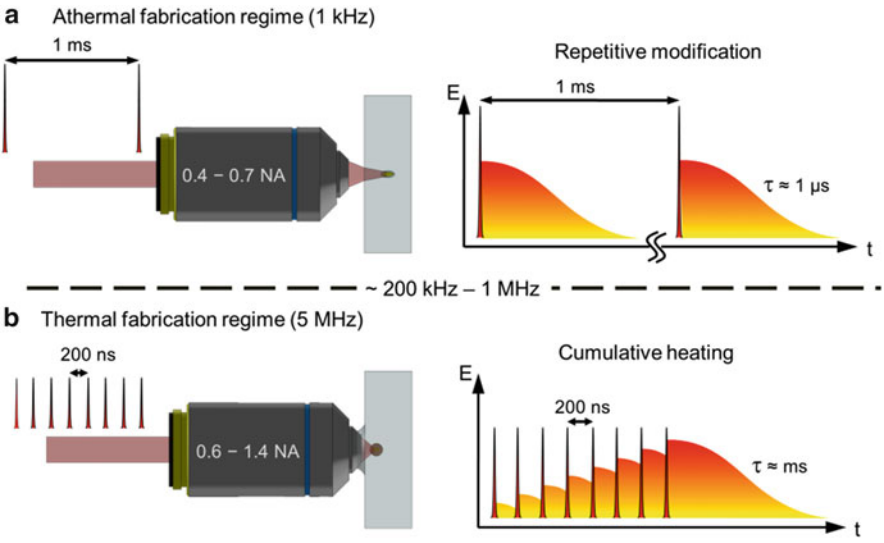

Fig. 4 (**a**) Nonthermal fabrication regime using low repetition rate and (**b**) thermal fabrication regime using high repetition regime (Gross and Withford 2015)

the size of melted volume can be controlled by the number of pulses N from laser exposure. Note that N can be expressed by $N = dR/v$, where d, R, and v are the spot size diameter (typically, $1/e^2$ of intensity), the repetition rate of the laser, and the scan speed of the translation stage, respectively. For cumulative heating, the morphology of the structural change is dominated by the heating, melting, and cooling dynamics of the material in and around the focal volume (Itoh et al. 2006).

Propagation Conditions

It is well known that linear effect includes dispersion, diffraction, and aberration during the light propagation in a medium. Typically, due to the large beam size (~3 mm), the intensity directly from the fs laser output port is not sufficient to achieve optical breakdown (~10^{13} W/cm^2) in transparent materials; as a fact, focused fs laser pulses are needed to obtain a small focal spot (micrometer-sized) via an external lens, resulting in a much higher laser intensity within the focal volume.

Before focusing inside the transparent materials, the spherical aberration and nonlinear propagation effects (i.e., self-focusing, self-phase modulation, etc.) can be ignored. The spatial intensity profile of an fs laser beam can be well represented by the paraxial wave equation and Gaussian optics. The intensity distribution of a Gaussian beam is:

$$I\,(r,z) = I_0\left(\frac{\omega_0}{\omega(z)}\right)^2 \exp\left(-\frac{2r^2}{\omega^2(z)}\right) \tag{5}$$

where the radial distance from the optical axis is $r = \sqrt{x^2 + y^2}$ and z is the axial distance from the beam waist and $I_0 = I(0,0)$ is the intensity at the center of the beam's tightest focus.

The waist radius is:

$$\omega(z) = \omega_0\sqrt{1 + \left(\frac{z}{z_0}\right)^2} \tag{6}$$

where ω_0 denotes the diffraction-limited minimum waist radius for a collimated Gaussian beam after focusing with lens characterized by NA and expressed by

$$\omega_0 = \frac{M^2\lambda}{\pi \mathrm{NA}} \tag{7}$$

where M^2 is the factor for non-perfect Gaussian beam (also indicating the beam quality), NA is the numerical aperture of the focusing microscope objective, and λ is the laser wavelength in free space. The Rayleigh range z_0 inside a transparent material with refractive index of n is given by:

$$z_0 = \frac{M^2\lambda n}{\pi \mathrm{NA}^2} \tag{8}$$

In our case, a Ti:sapphire fs laser with the bandwidth of ∼10.7 nm was applied for micromachining; such small value can reduce the effect of chromatic aberration caused by dispersion. Of course, one can employ a chromatic aberration-corrected microscope objective for the wavelength spectrum of interest, such as $\lambda = 800$ nm in our case. For the issue of spherical aberration coming from spherical shape of lens, it can be addressed by using multiple lenses (i.e., microscope objectives) or an aspherical focusing lens.

If the laser beam is focused inside the transparent materials, the light propagating through the air-glass interface (flat) may introduce additional spherical aberration. Even worse condition may happen with respect to optical fibers with curvature interface. Therefore, a common way of addressing this issue is employing an oil immersion microscope objective with the refractive index of matching oil equals to that of transparent materials.

In addition to the linear propagation, nonlinear effects can also happen when the laser intensity within the focal point inside the transparent materials is extremely high. Typically, the propagation of light in a medium is governed by Maxwell's equation:

$$\begin{aligned} \nabla \times E &= -\frac{\partial B}{\partial t} \\ \nabla \times H &= -\frac{\partial D}{\partial t} + J \\ \nabla \cdot D &= q \\ \nabla \cdot B &= 0 \end{aligned} \tag{9}$$

where q is the free charge density, J is the current density vector, **E** and **H** are the electric and magnetic field vectors, respectively, and **D** and **B** are the displacement vectors given by

$$\begin{aligned} D &= \varepsilon_0 E + P \\ B &= \mu_0 H + M \end{aligned} \tag{10}$$

where μ_0 is the permeability of free space. **P** and **M** are the laser-induced electric and magnetic polarizations, respectively. In our cases (i.e., fused silica and sapphire), $\mathbf{M} = 0$, indicating nonmagnetic dielectrics. J and q are also equal to 0 when the light is propagating in a dielectric. So the wave equation can be derived from Eqs. 9 and 10:

$$\nabla \times \nabla \times E + \frac{1}{c^2}\frac{\partial^2}{\partial t^2} E = -\mu_0 \frac{\partial^2}{\partial t^2} P \tag{11}$$

where $c = 1/\sqrt{\mu_0 \varepsilon_0}$ is the speed of light in vacuum.

When light propagates through a dielectric material, it induces microscopic displacement of the bound charges, forming oscillating electric dipoles that add up to the macroscopic polarization which for glass with inversion symmetry is given by:

$$P = \varepsilon_0 \chi^{(1)} E + P^{\mathrm{NL}} = \varepsilon_0 \left[\chi^{(1)} + \frac{3}{4} \chi^{(3)} |E|^2 \right] E \tag{12}$$

where $\chi^{(i)}$ is the ith order susceptibility, with $\mathrm{P}^{(2)}$ and $\mathrm{P}^{(n)}$, where $n \geq 3$ left out of Eq. 12 due to even-order symmetry and negligible contribution when laser intensity is not extremely high. The refractive index can be identified from Eq. 12 as (Shen 1984):

$$n = \sqrt{1 + \chi^{(1)} + \frac{3}{4} \chi^{(3)} |E|^2} = n_0 + n_2 I \tag{13}$$

where $n_0 = \sqrt{1 + \chi^{(1)}}$, $n_2 = 3\chi^{(3)}/4\varepsilon_0 c n_0^2$, and $I = \frac{1}{2}\varepsilon_0 \mathrm{cn}_0 |E|^2$ are the linear refractive index, nonlinear refractive index, and the laser intensity. A nonzero nonlinear refractive index n_2 (optical Kerr effect) gives rise to many nonlinear optical effects as an intense fs laser pulse propagates through transparent materials.

The Kerr nonlinearity $\chi^{(3)}$ results in an intensity-dependent refractive index change that follows the spatial intensity profile (i.e., Gaussian) of the laser. A Gaussian intensity profile results in the evolution of a positive or negative lens, depending on the sign of the nonlinear refractive index n_2. In the fs laser direct writing regime, n_2 is a positive value for most transparent materials. If the laser intensity is high enough, term $n_2 I$ in Eq. 13 plays a significant role to the refractive index n of the material, leading to focusing the light as passing through a positive lens. The phenomenon is also called self-focusing nonlinear effect. The strength of self-focusing depends only on the peak power of the laser, and the critical power for self-focusing can be expressed by (Shen 1984):

$$P_{\mathrm{cr}} = \frac{3.77\lambda^2}{8\pi n_0 n_2} \tag{14}$$

Obviously, if the peak power (P) of the fs laser pulse exceeds P_{cr}, the collapse of the pulse to a focal point is predicted. In addition, the initial point of self-focusing occurs at (Shen 1984):

$$Z_f = \frac{2n_0}{0.61} \frac{\omega_0}{\lambda} \frac{1}{(P/P_{\mathrm{cr}})^{1/2}} \tag{15}$$

Nevertheless, due to the free electron plasma formation at the focal point, such laser-induced plasma also has a defocusing effect for fs laser pulse propagation and can modify the real part of the refractive index as (Shen 1984):

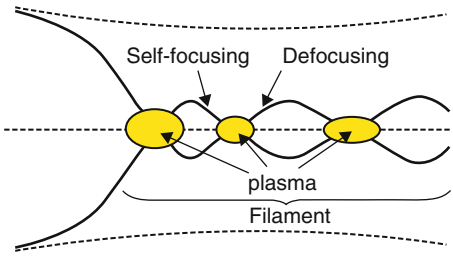

Fig. 5 Schematic representation of the focusing-defocusing cycles undergone by the intense center of a laser beam (Couairon and Mysyrowicz 2007)

$$n = n_0 - \frac{n(t)}{n_0 n_c(t)} \tag{16}$$

where $n_c(t)$ is the characteristic plasma density for which the plasma frequency equals to the laser frequency obtained from Eq. 3. The plasma-modified refractive index (Eq. 16) acts as a diverging lens to the laser beam and counters the Kerr lens self-focusing (Eq. 14). Such mechanism will always balance self-focusing and prevent pulse collapse inside transparent materials (Couairon and Mysyrowicz 2007), as shown in Fig. 5. In our cases, self-focusing is usually avoided in micromachining by tightly focusing the laser beam with an appropriate microscope objective to reach the intensity for optical breakdown ($\sim 10^{13}$ W/cm^2) without exceeding critical power for self-focusing. Typically, in fused silica, the critical power is $\sim$1.8 MW for the laser wavelength $\lambda = 800$ nm, $n_0 = 1.45$, and $n_2 = 3.5\times10^{-20}$ m^2/W (Sudrie et al. 2002).

Laser Processing System for Direct Writing in Optical Fiber

Femtosecond Laser Micromachining System

The optofluidic/ferrofluidic devices presented in this chapter are fabricated with our home-integrated fs laser micromachining system. The schematic of the system with direct writing capability is shown in Fig. 6. The full ultrafast laser system consists of a diode-pumped solid-state laser with high power CW output at 532 nm (Verdi V18, Coherent Inc.), a Ti:sapphire mode-locked laser (Mira 900, Coherent Inc.), and a Ti:sapphire regenerative amplifier laser (RegA 9000, Coherent Inc.). As mentioned above, such system was used for transparent material processing. The central wavelength, pulse width, and repetition rate of the fs laser are set at 800 nm, 200 fs, and 250 kHz, respectively. The maximum output power of the fs laser is 1 W.

A half-wave plate in combination with a Glan-Thompson calcite polarizer is used to precisely control the actual power used for fabrication, while an optional variable neutral density (ND) filter is used to tune the laser power more precisely. The laser exposure is switched on or off by an external mechanical shutter (SH05, Thorlabs) or electrically gating the internal clock via laser controller. In general case, the laser

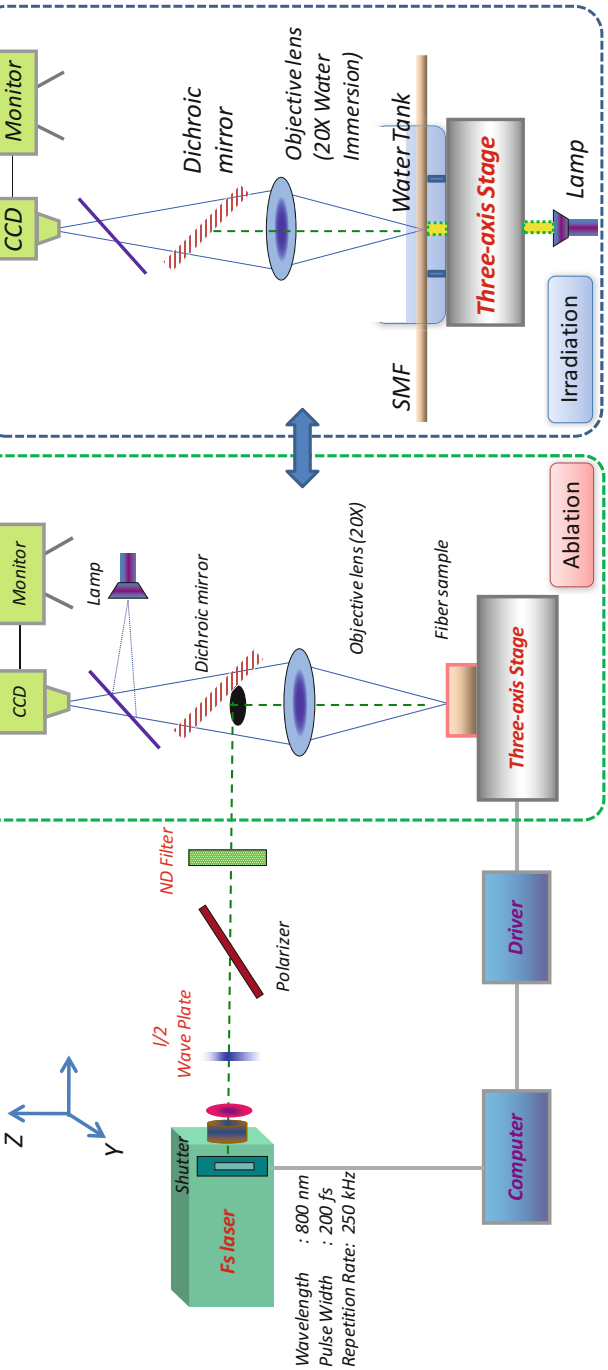

Fig. 6 Schematic diagram of the fs laser micromachining system

beam is passed through a commercial microscope objective to create a tightly focused spot. The actual laser energy used for processing silica glass and single crystal sapphire is approximately 0.4–0.5 μJ per pulse, respectively.

Silica glass substrates or optical fiber samples are mounted on a computer-controlled three-axis translation stage (PM500 series, Newport, Inc.) with a resolution of 0.1 μm. According to different fabrication cases, fiber mounting methods and illumination choices vary subsequently, so are the velocities of the translation stage. Details can be found in the following chapters. In our case, the fs laser beam is directly focused on the fiber surface (ablation) through an objective lens (20X) with a NA of 0.4 or focused inside the fiber sample (irradiation) using a water immersion lens (20X) with a NA of 0.4 or an oil immersion lens (100X) with a NA of 1.3. The diameter of the focused beam is varied from 0.5 to 1 μm with respect to different microscope objectives. A dichroic mirror and a charge-coupled device (CCD) camera connected to the computer are involved to in-situ monitor the fabrication process. Front-side and backward illumination methods can be used for different fabrication purposes. For example, both methods are suitable for transparent material ablation/irradiation, while for the nontransparent materials (i.e., silicon), only front-side method is acceptable.

During the laser processing of transparent materials, exposure conditions such as pulse energy, repetition rate, scanning speed, beam shape condition (spatio/temporal beam profile), and polarization state have significant impacts on the micromachined structures. For example, the polarization state of the laser beam can be well controlled using the combination of a half-wave plate and a polarizer, which is useful for nanostructure formation (Bhardwaj et al. 2006). Although such existing schematic is only used for low-throughput application, compared with parallel processing via spatial light modulator (SLM) (Wang et al. 2015), it is still suitable for most of research levels under laboratory conditions. Details of fs laser system and beam delivery path can be found in Fig. 7.

The movement of the three-axis translation stage can be well controlled through a home-developed graphical user interface (GUI) software based on MatLab.

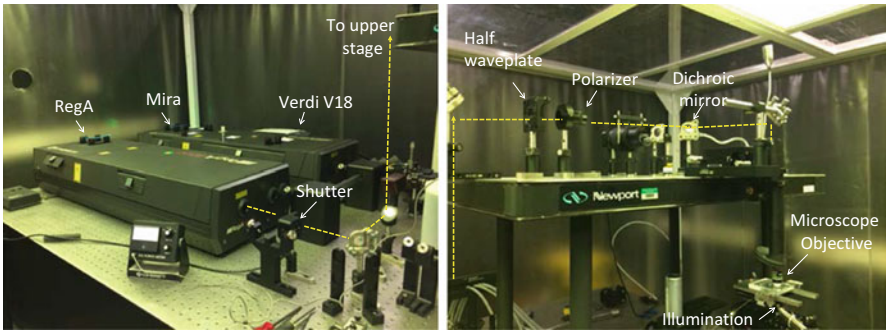

Fig. 7 Fs laser system and beam delivery path

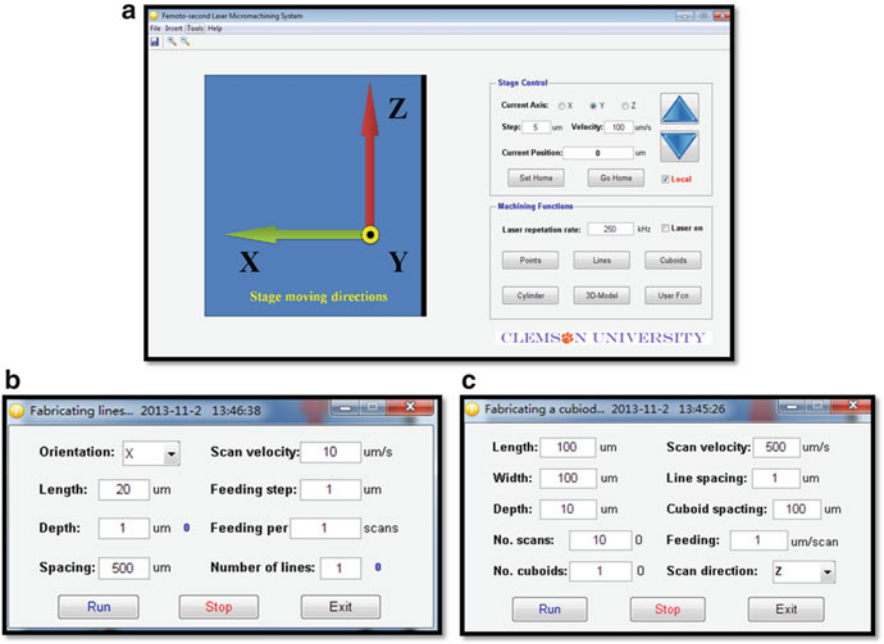

Fig. 8 Interfaces of the developed software. (**a**) Main GUI, (**b**) inscribing lines, and (**c**) fabricating cuboids

GPIB-USB connection method is adopted for the communication between the stage controller and a desktop. Multifunctional operations (i.e., stage control and machining functions) are involved within this software, showing great capabilities for complex structure micromachining. Details of the interfaces of this proposed software are shown in Fig. 8a–c.

Direct Femtosecond Laser Writing in Optical Fiber

Since we are mainly focusing on laser direct writing in optical fibers, two standard writing geometries can be applied for different purposes, including longitudinal mode and transverse mode, as shown in Fig. 9.

In longitudinal writing mode, the optical fiber is horizontally placed on a multi-axis translation stage, moving vertically either toward or away from the incident laser. Due to the transverse symmetry Gaussian intensity of the laser beam, the modifying structures have cylindrical symmetry. However, such configuration is highly depending on the working distance of the focusing lens, resulting in a short length of modifying structures.

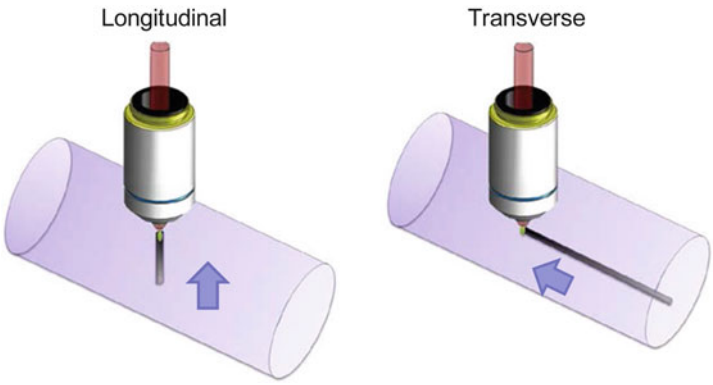

Fig. 9 Laser direct writing geometries in optical fibers, including longitudinal mode and transverse mode

In most cases, people employ transverse mode for waveguide direct writing (Davis et al. 1996), in which the writing direction is perpendicular to the laser propagation direction. The working distance is no longer an issue for this configuration, and 3D optical circuits can be realized using this method. However, the cross section of modifying structure is asymmetric (elliptical) due to the ratio between the focal depth ($2z_0$) and spot size ($2\omega_0$), which is related to the following relationship $2z_0/2\omega_0 = n/\text{NA}$. To overcome this issue, using high NA objective lens is helpful, such as oil immersion lens.

The spot size of the focal point inside the transparent materials plays a significant role for high accuracy, high-precision 3D structure micromachining using fs laser. Typically, the radius r of the spot size can be roughly calculated by (Gamaly et al. 2006):

$$r = \frac{0.61}{\text{NA}}\frac{\lambda}{n} \tag{20}$$

Here, λ is the wavelength of incident laser, and λ/n means the effective wavelength when the laser is focused inside media of index n. As such, the focal spot inside material is smaller by factor n than that in air ($n_{air}=1$). Obviously, once the wavelength of the laser and the refractive index of the material are fixed, r only depends on the NA of microscope objective. The larger the NA is, the smaller the spot size will be. In general, low NA (<0.1) microscope objective is used for large-area surface modification. Lenses with NAs from 0.1 to 0.5 can induce a confined permanent modification inside a transparent material or ablate the surface of materials with high precision. The immersion lenses (water immersion or oil immersion) usually have even larger NAs (NA > 0.9). The immersion optics not only tightly focused the laser beam but also compensates refractive index mismatch

Table 1 The pros and cons of each microscope objective

Microscope objective	Pros	Cons
20X (Zeiss EC Epiplan)	Small NA (0.4)	Not suitable for laser irradiation inside optical fibers
	Suitable for laser ablation with high precision	
20X water immersion (Olympus)	Less spherical aberration	Filament issue when used at high power; large spot size
	Suitable for laser-induced weak reflector/stresses	
60X water immersion (Olympus)	Small laser spot size	Limited working distance
	Laser-induced water breakdown	Spherical aberration
100X oil immersion (Olympus)	Small laser spot (~0.5 μm)	Limited working distance
	No spherical aberration high precision	Complicated operation

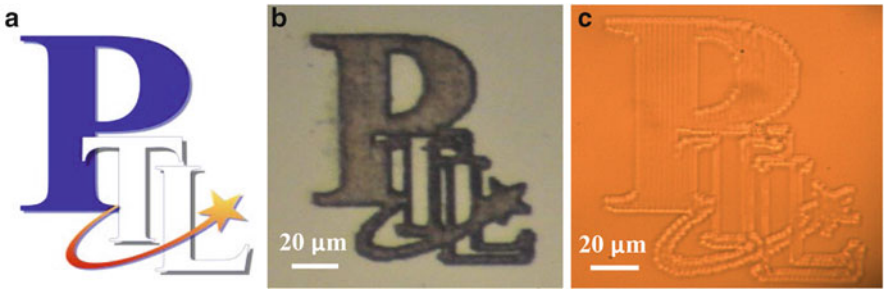

Fig. 10 The logos of Photonics Technology Lab. (**a**) Original file, (**b**) laser ablated on the surface of silica glass, and (**c**) laser irradiated inside the silica glass

at the surface of the sample. As a result, material can be modified with a tightly focused fs laser pulses even at the nJ energy level.

For different fabrication purposes, four types of microscope objectives are chosen in this work. The pros and cons of each microscope objective are discussed, as shown in Table 1.

With the proposed fabrication system, a lot of fancy and complex structures can be realized. Examples include Photonics Technology Lab (PTL) logos displayed on the surface and inside the silica glass (Fig. 10), helical shape formation inside a silica fiber (Fig. 11), line-by-line grating inscription inside a sapphire fiber (Fig. 12), and micro-cantilever beam ablated on the tip of a silica fiber (Fig. 13).

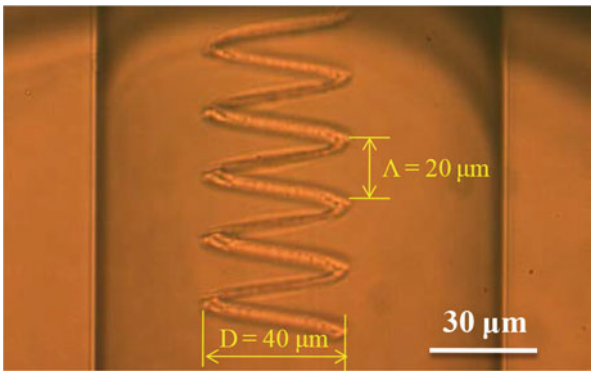

Fig. 11 Helical structure in a silica fiber. Pitch $\Lambda = 20\ \mu m$ and diameter $D = 40\ \mu m$

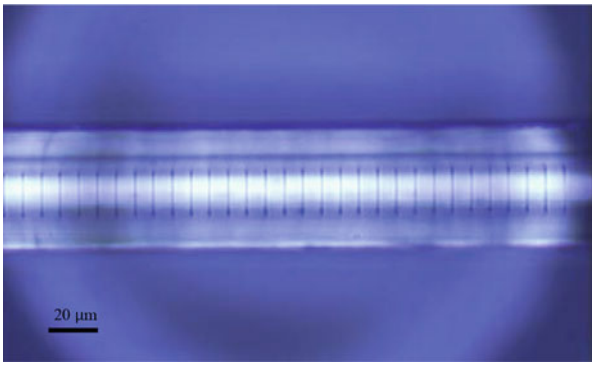

Fig. 12 Line-by-line grating inscription inside a sapphire fiber

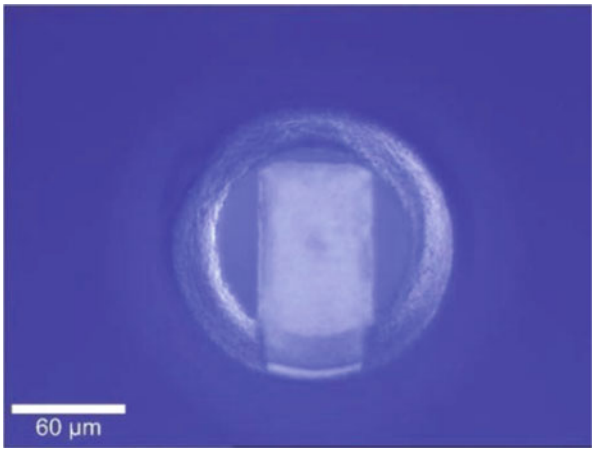

Fig. 13 Micro-cantilever structure ablated on the tip of silica fiber

Liquid-Assisted Laser Processing in Optical Fiber

Introduction to Liquid-Assisted Laser Processing

Recent technological advances have led to the development of optofluidic-based systems, in which waveguide and microfluidic architectures are synergistically integrated to provide enriched intelligence and enhanced functionalities for chemical and biological sensing applications (Schaffer et al. 2001). In an optofluidic system, buried microchannels can be formed in solid or soft transparent materials (i.e., silica or PMMA) through advanced manufacturing techniques. The liquid of interest (in a small volume) confined and manipulated inside the microchannels can be probed and analyzed using optical measurements (Yablonovitch and Bloembergen 1972).

In addition to the well-known planar configurations of optofluidic systems, the idea of all-in-fiber optofluidic devices (i.e., PCF-based and OFRR-based) has also been investigated (Glezer and Mazur 1997; Stoian et al. 2000). Additionally, taking advantage of fs laser micromachining technique in transparent materials, the alignment-free optics and improved robustness of all-in-fiber optofluidic devices have been proposed in the past years. Existing methods can be classified into two categories: (1) fs laser irradiation with chemical etching (i.e., HF or KOH), also known as FLICE technique, and (2) fs laser-induced water breakdown (FLIWD) technique.

In 2006, Y. Lai et al. from Bennion's group firstly demonstrated a microchannel formed in an SMF using FLICE for refractive index sensing application (Rethfeld et al. 2004). The intensity change as a function of refractive index variation was investigated. Later, their group created microfluidic networks in fiber cladding of SMFs using FLICE technique and made this device as a sensor for temperature and refractive index sensing applications (Zhou et al. 2010). However, due to the high roughness on the surfaces of microchannels, large optical insertion losses could exist. Recently, researchers from Hermann's group have improved the roughness on the FLICE-formed surfaces down to 10 nm (rms) in bulk fused silica (Ho et al. 2012) and presented an intricate and highly compact lab-in-fiber sensors fabricated by laser direct writing waveguides and FLICE techniques with a variety of functionalities, such as fluorescence, temperature, refractive index, and bending sensing applications (Haque et al. 2014). However, the uniformity (taper angle involved) of the long-length channel is an issue when using HF as etchant due to the etch selectivity between the laser-irradiated region and unexposed region. Although KOH solution can significantly enhance the etch selectivity, the etch rate is much lower than that of HF (Kiyama et al. 2009).

In addition to FLICE technique, a microchannel can be directly created in an SMF using FLIWD technique without using any toxic or hazard chemical solutions (Liu et al. 2013). Such device can be used for temperature and RI sensing applications. In this process, the interaction between the laser and the liquid (i.e., DI water) can cause the laser-induced water breakdown phenomenon with laser-induced bubbles, shockwaves, and a high-speed jet. Meanwhile, the water plays a significant role to efficiently remove debris from the ablated regions, resulting in the

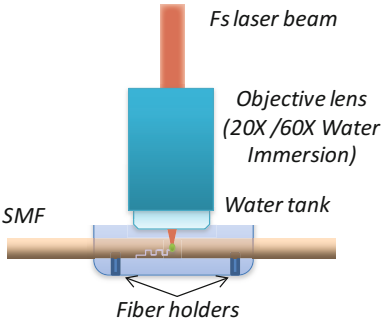

Fig. 14 Schematic of FLIWD for the fabrication of 3D arbitrary microchannels in an optic fiber

formation of microfluidic channels with arbitrary shapes. The schematic diagram of FLIWD for the fabrication of 3D microchannels in an SMF can be found in Fig. 14. Compared to FLICE, this technique can provide better uniformity of the channel diameter, which is mainly depending on the spot size of the laser beam (or the NA of objective lens). However, when the length of the microchannel reaches several hundreds of micrometers, the debris generated by fs laser ablation is hard to be washed out using water, which restricts the length of the fabricated microchannels (typically ∼1 cm An et al. 2005). Additionally, the low-quality surface profiles can generate significant optical insertion loss, and relative low translation speed (∼1 to 2 μm/s Liu et al. 2013) may cause time-consuming concern.

Fabrication of 3D Hollow Structure in Optical Fibers

Both FLIWD and FLICE can be used to fabricate 3D hollow structure in optical fibers. FLIWD technique is firstly investigated here. Figure 15a shows the schematic FLIWD micromachining system. The actual laser energy used for fabrication was approximately 0.8–1.2 μJ per pulse for low NA lens, which is much higher than the threshold of fused silica. Figure 15b shows the details of FLIWD fabrication process.

The fiber used in experiments was a single-mode optical fiber (Corning, SMF-28e) with the core and cladding diameters of 8.2 and 125 μm, respectively. After mechanically stripping off its buffer, the fiber was cleaned using acetone and clamped onto two bare fiber holders (Newport 561-FH). The optical fiber and fiber holders were immersed in distilled water during fabrication. The fiber assembly was mounted on a computer-controlled three-axis translation stage (Newport, Inc.) with a resolution of 0.1 μm. The fs laser beam was focused inside the optical fiber through a water immersion objective lens (Olympus UMPlanFL 20×/60×) with a numerical aperture (NA) of 0.4 or 0.9, respectively. The spot size of the focused beam was about 5 μm in fiber due to the much higher pulse energy for 20x lens, while for 60x lens, the spot size can be reduced down to 2 μm with the pulse energy of 0.4 μJ. The velocities of the stages were set at 1 μm/s during fabrication.

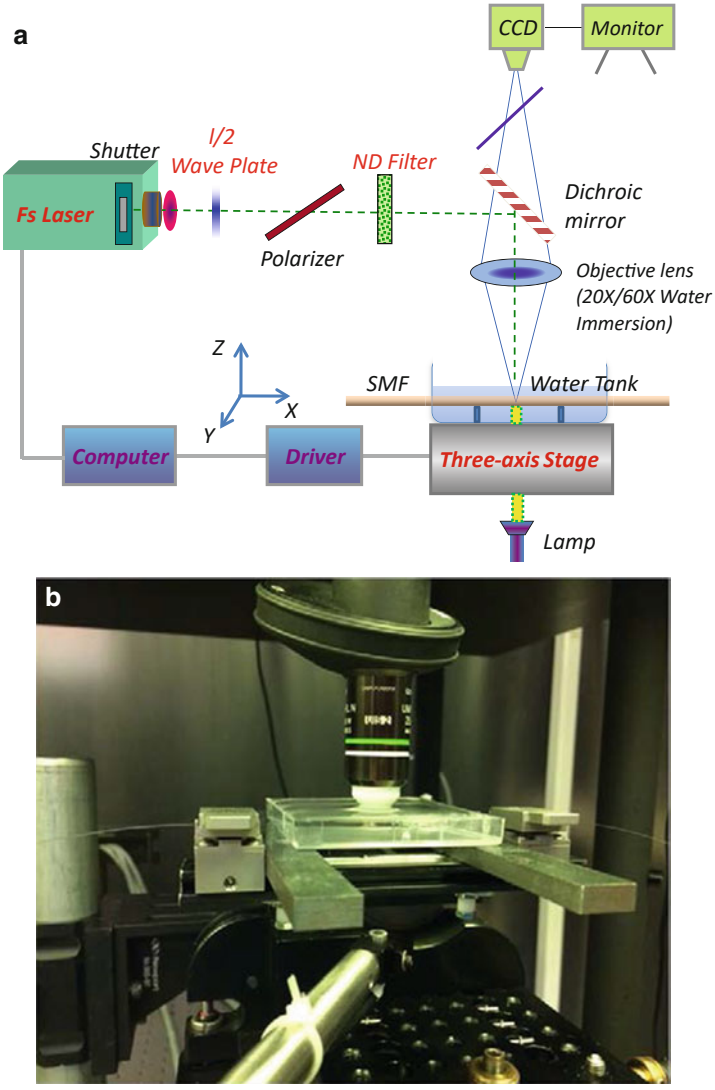

Fig. 15 (**a**) Block diagram of FLIWD for the fabrication of 3D arbitrary microchannels in an optic fiber. (**b**) Figure of details of FLIWD experiment setup

A straight microchannel with the diameter ~5 μm was fabricated in the x-y plane using FLIWD method, and the microscope image is shown in Fig. 16. Obviously, the roughness of the microchannel surface is not smooth enough, which means the optical insertion loss might be extremely high. If higher NA microscope objective was adopted, the result can be significantly improved. However, high NA lens is hard to operate and easy to be affected by spherical aberration issue.

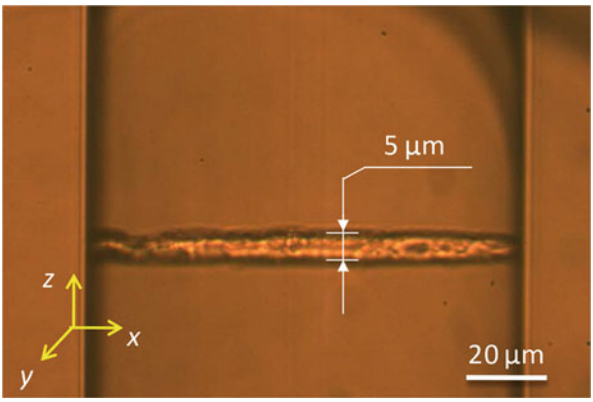

Fig. 16 Microscope image of a straight microchannel inside an SMF fabricated by FLIDW technique

Alternatively, FLICE technique was investigated to get a better result for the fabrication of 3D hollow structure inside an optical fiber. The block diagram of FLICE technique is much similar to laser irradiation micromachining system. In this case, the fs laser beam can be focused inside the optical fiber through either a water immersion objective lens (Olympus UMPlanFL 20×) with a numerical aperture (NA) of 0.4 or an oil immersion lens (Olympus UMPlanFLN 100X, NA = 1.3) with the index-matching oil of RI = 1.464 (Cargille Laboratories). The actual laser energy used for fabrication was approximately 0.4 μJ or 0.2 μJ per pulse for two different microscope objectives. So the spot size of the focused beam was about 2 μm or 0.5 μm in fiber. The velocities of the stages were set at 10–50 μm/s during fabrication. After laser irradiation, the fiber was well cleaned in acetone solution and DI water to fully remove the residue index-matching oil. Then the HF etching process was conducted. This technique offers great simplicity and flexibility to produce buried 3D structures with high aspect ratios in transparent materials (Bellouard et al. 2004). The etching rate of a laser-modified region was found to be two orders of magnitude higher than that of the unexposed region in silica materials. As a result, such hybrid technique has been adopted for fabrication of optofluidic devices in planar sample and optical fibers (Crespi et al. 2010).

It should be noticed that the etching rate in the germanium-doped core of the SMF is much faster than that in the fiber cladding. The respective reactions can be found as follows (Tuck et al. 2006):

$$SiO_2 + 4HF \rightarrow 2H_3O^+ + SiF_6{}^{2-} \tag{21}$$

$$GeO_2 + 4HF \rightarrow 2H_3O^+ + GeF_6{}^{2-} \tag{22}$$

The reactions are driven by different dissociation energies of the Si-O bond (799.6 kJ/mol) and Ge-O bond (660.3 kJ/mol) (Gong et al. 2009). Therefore, smaller pulse energy is needed in fiber core for exciting the electrons from valence band to conduction band, leading to a concave surface profile inside the fiber core during HF etching process. One possible solution is using HF solution (Acros Organics) with

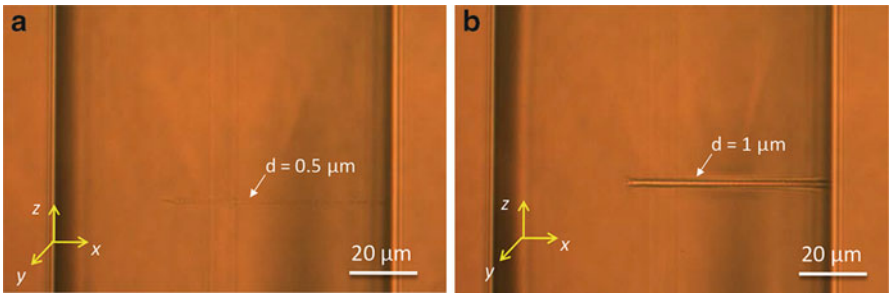

Fig. 17 Microscope images of a blind microhole inside an SMF fabricated by FLICE technique. (**a**) Before HF etching and (**b**) after HF etching

low concentration (i.e., 5%) for the etching of microchannels in SMFs. However, there is a trade-off between the quality of the channel and the consuming of the time. Typically, lower concentration of HF etchant will consume longer time, and then a better quality of microchannel will be formed and vice versa. Actually, by using HF solution as etchant solely, the etching rate difference between the fiber core and cladding is quite small due to the low doping concentration of GeO_2 in SMFs.

Here is an example to show how we can use FLICE to fabricate a blind microhole inside an SMF. High NA (1.3) oil immersion objective was used for laser irradiation, and low NA (0.4) water immersion lens was adopted for quality check. After laser irradiation, the fiber was cleaned with acetone and DI water and then etched with 5% aqueous HF solution for approximately 15 mins to fully open the blind microhole. Figure 17a shows the laser-irradiated structure before etching, and Fig. 17b shows the blind microhole formed inside the SMF after HF etching process. The diameter of the microhole is about 1 μm. In addition, we cannot see obvious difference between fiber core and cladding after HF etching. The proposed example indicates the potential of fabricating high-quality 3D hollow structure inside SMFs using our fs laser micromachining system.

All-in-Fiber Optofluidic Sensor

In this section, an assembly-free, all-in-fiber optofluidic sensor was proposed as an example for RI sensing in optofluidic systems. FLICE technique was adopted for the fabrication of such advanced fiber-optic sensor.

Operation Principle and Sensing Mechanism

The fs laser ablation technique has been used to micromachine FP cavities on optical fibers for various sensing applications such as RI (Wei et al. 2008) and pressure (Zhang et al. 2013) measurement. It has been proven that the formed

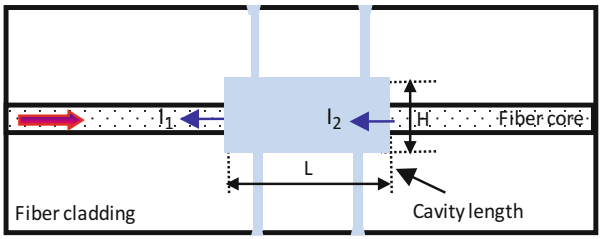

Fig. 18 Schematic of the all-in-fiber optofluidic device

FP cavity is insensitive to the ambient temperature. However, it was also found that the open cavity structure (Wei et al. 2008) was sensitive to fiber bending and easy to break. Here, we propose a prototype all-in-fiber 3D optofluidic microdevice fabricated by the FLICE technique. The FLICE technique has been proven for rapid fabrication of embedded 3D channels with flexible orientations inside an optical fiber (Fig. 17a, b). To demonstrate the feasibility, we fabricated and tested all-in-fiber optofluidic devices consisting of horizontal and vertical microchannels. The horizontal microchannel can be conceived as a FP cavity, while the vertical ones are the inlets/outlets to the cavity.

Figure 18 illustrates the schematic of the prototype all-in-fiber optofluidic device, where a horizontal fluid-holding cavity is embedded in the center of a single-mode fiber and four vertical microchannels are punched through the fiber cladding to allow liquid access to the cavity. The device is fabricated in two steps: (1) irradiation of the selected regions (the rectangular cavity and vertical channels) with focused fs laser pulses and (2) selective etching of the laser-modified zones using the HF solution.

Optically, the horizontal cavity also functions as a FP cavity. The light propagates inside the fiber and reflects at the two air/silica endfaces of the cavity. The light intensities of the reflected beams by the two surfaces of the FP cavity are denoted as I_1 and $I_2 I_2$, respectively, superimpose to generate an interference pattern. The FP interferometer can be modeled using the following two-beam optical interference Eq. 20:

$$I = I_1 + I_2 + 2\sqrt{I_1 I_2}\cos\left(\frac{2\pi \cdot \mathrm{OPD}}{\lambda} + \phi_0\right) \tag{21}$$

where I is the intensity of the interference signal, ϕ_0 is the initial phase of the interference (normally equal to zero), and λ is the optical wavelength in vacuum. The round-trip OPD of the FP interferometer is given by:

$$\mathrm{OPD} = 2n_{\mathrm{cavity}}L \tag{22}$$

where n_{cavity} is the RI of the cavity medium and L is the length of the cavity length. At the valleys of the interferogram in spectrum domain, the phase difference of the two reflected light beams satisfies the condition of coherently destructive interference:

$$\frac{4\pi n_{\text{cavity}} L}{\lambda_m} + \phi_0 = (2m+1)\,\pi \tag{23}$$

where m is an integer and λ_m is the wavelength of the mth order interference valley. For two adjacent wavelength minima, the following condition is obtained:

$$\frac{4\pi n_{\text{core}} L}{\lambda_1} - \frac{4\pi n_{\text{core}} L}{\lambda_2} = (2m+1)\,\pi - [2\,(m+1)+1]\,\pi = 2\pi \tag{24}$$

The distance between two adjacent minima of the spectrum, defined as free spectrum range (FSR), can then be expressed as:

$$\text{FSR} = \frac{\lambda^2}{2n_{\text{cavity}} L} \tag{25}$$

According to Eq. 23, taking the derivative of n with respect to λ_m, one finds:

$$\frac{d\,n}{d\,\lambda_m} = \frac{[(2m+1)\,\pi - \phi_0]}{4\pi\,L} \tag{26}$$

Assuming the cavity length L is maintained constant during measurement, Eq. 26 indicates that the RI is a linear function of the wavelength at interference valley, and then the sensitivity of the FP interferometer is a constant. The amount of RI change (Δn) can thus be computed based on the wavelength shift of a specific interference valley using the following equation:

$$\frac{\Delta n}{n} = \frac{\Delta \lambda_m}{\lambda_m} \tag{27}$$

where the relative RI change is directly proportional to the spectral shift of the interferogram.

Sensor Fabrication

In order to fabricate a high-quality FP cavity, the following steps were adopted. First, a rectangle region, with the dimension of $L\times 10 \times H$ μm, was inscribed in the center of the fiber using fs irradiation from the bottom to the top (z direction, as shown in Fig. 15a), where L and H denote the length and height of the micro-cavity, respectively. The center of the inscribed region is aligned with the center of the fiber core. Second, the irradiation position of the vertical channels was chosen. The laser was initially focused at the center of the fiber core. Then the stage was moved along the z direction to make sure the fs laser beam can irradiate a straight line along the z direction. After one-side fabrication, the fiber was then rotated by 180° to

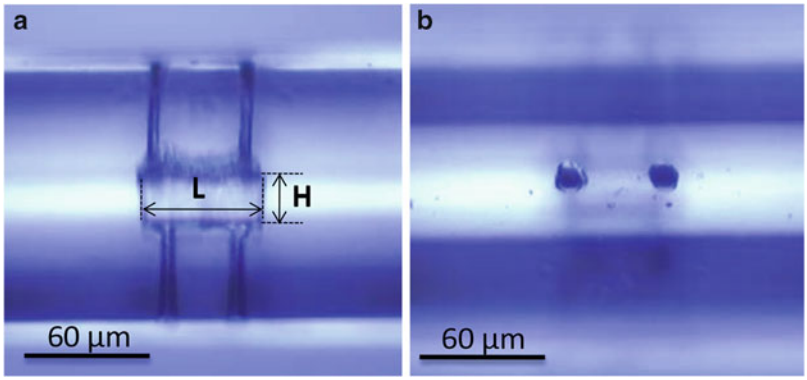

Fig. 19 (**a**) Microscope image of the fabricated all-in-fiber optofluidic device: the length L and the height H of the FP cavity are 55 and 20 μm, respectively. (**b**) Top view of the fiber device

fabricate the channels on the other side following the same procedure. After fs laser irradiations, the sample was dipped into a HF solution with a concentration of 20% for about 10 min. The actual etching time may depend on the HF concentration and cavity dimensions. As the final step, the etched sample was cleaned in an ultrasonic bath filled with distilled water and dried in air. The embedded cavity was close to the end of the fiber to minimize the possibility of device breakage due to fiber bending.

Figure 19a shows the microscope image of a fabricated all-in-fiber optofluidic device, where the cavity length L and the cavity height H are about 55 μm and 20 μm, respectively. Figure 19b shows the top view of the device. The diameter of the vertical microchannels is about 5 μm.

The fabricated all-in-fiber optofluidic device was interrogated using a broadband light source with wavelength range from 1520 to 1620 nm. A 3 dB fiber coupler was used to route the light into and out of the device. The interference spectrum was recorded by an OSA (AQ6319). Figure 20 shows the reflection spectra of the all-in-fiber optofluidic device with the FP cavity length of 35 μm and 55 μm, respectively. The FSRs of these two interferometers are 36 nm and 21 nm, respectively, which matched well with those calculated using Eq. 25. The clean interference pattern with a large fringe visibility of 20 dB was obtained with the cavity length of 55 μm. The device with 35 μm of cavity length had a fringe visibility of about 12 dB. The excess losses of both devices were about 18 dB, which was mainly caused by the roughness of the cavity surfaces. To a certain extent, the surface quality can be improved by tuning the laser irradiation power, adjusting the concentration of HF solution (i.e., 5%) and the etching time (i.e., ∼45 mins).

Measurement of RI with the Optofluidic Sensor

The all-in-fiber optofluidic device with a cavity length of 55 μm was tested for its capability of RI measurement at room temperature. The vertically placed sensor

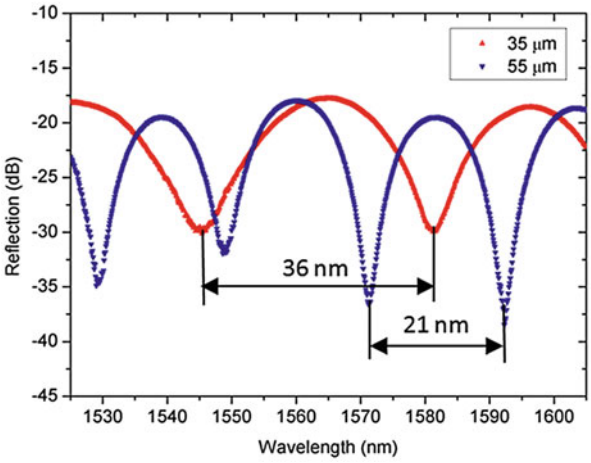

Fig. 20 Reflection spectra in air of the all-in-fiber optofluidic devices with cavity lengths of 35 and 55 μm, respectively

probe was directly immersed into the sucrose solutions with different concentrations of 0.00, 1.00, 2.00, 3.00, 4.00, 5.00, 6.00, 7.00, 8.00, and 9.00 (unit: percentage). The corresponding RIs are 1.3333, 1.3344, 1.3359, 1.3373, 1.3388, 1.3403, 1.3418, 1.3433, 1.3448, and 1.3463, respectively. The ultrasonic bath was used to assist the liquid to flow into the embedded FP cavity during tests and to ensure no air bubble left in the cavity. In each measurement cycle, the device was carefully cleaned using acetone and DI water and dried after each measurement to ensure there was no residual liquid left within the cavity, indicated by the interference spectrum restored to its original in air.

The time needed for ultrasonic bath-assisted sample loading was about 10 s. In comparison, it took about 16 min to load the cavity without the ultrasonic bath. It is worth noting that the purpose of this thesis is to demonstrate the potentials of using the FLICE technique to fabricate embedded 3D structures inside an optical fiber and the feasibility of integrating the fluidic channels with a fiber sensor toward optofluidic applications. It is envisioned that other microfluidic components can be fabricated on the surface or inside the optical fiber using the same technique to facilitate the fluidic transport and storage. When integrated with the extra fluidic components, the use of ultrasonic bath becomes unnecessary because the standard sample loading method, e.g., syringe pumping, shall be able to load the samples.

Figure 21a shows the interference spectra of all-in-fiber optofluidic device in the sucrose solutions at various concentrations of 0%, 2%, 4%, and 6%, respectively. As the RI increased, the interferogram shifted toward the long wavelength region (red shift). Figure 21b plots the center wavelength of an interference valley (1567.6 nm) as a function of the RI of the liquid. Linear regression was used to fit the response curve, and the slope of the fitted line was calculated as the RI sensitivity, which was estimated to be 1135.7 nm/RIU in the tested RI range. Similar responses were obtained using the device with the cavity length of 35 μm. The length of the cavity should be limited to several hundred microns to avoid the excess optical

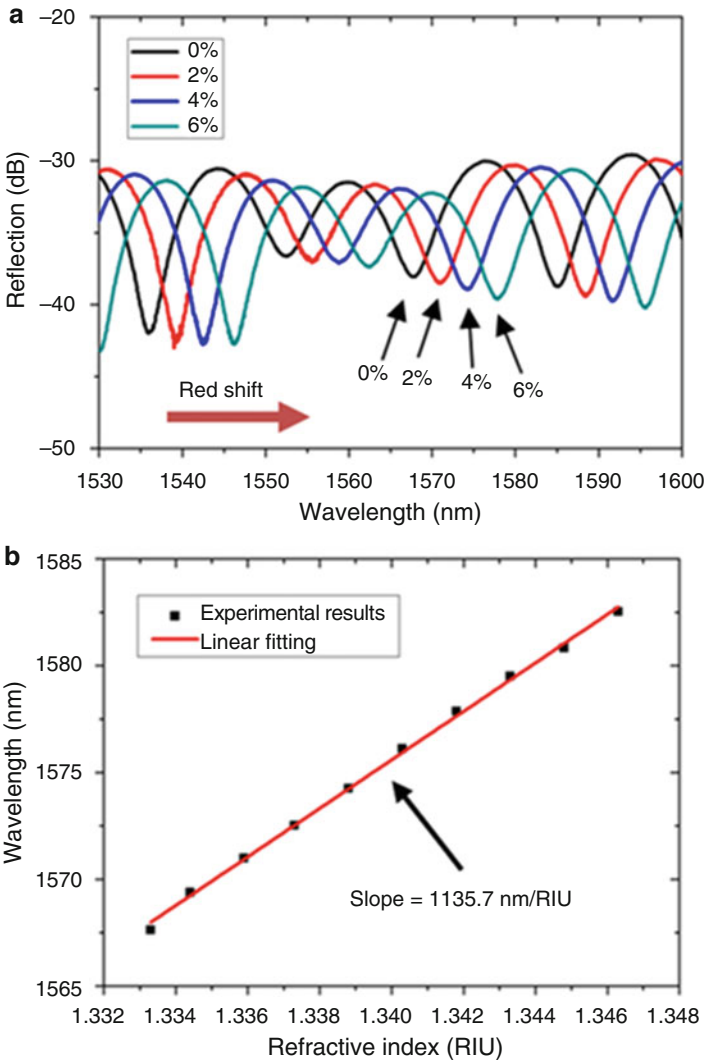

Fig. 21 (**a**) Interference spectra and (**b**) center wavelength of an interference valley (1567.6 nm) of the all-in-fiber device in sucrose solutions with different concentrations

loss caused by the divergence of the optical beam propagating inside the FP cavity (Zhang et al. 2010).

In summary, an all-in-fiber 3D optofluidic microdevice was fabricated by fs laser irradiation-assisted selective chemical etching. The proposed all-in-fiber optofluidic device is flexible in design, simple to fabricate, mechanically robust, and miniaturized in size, showing good potentials for chemical/biomedical sensing and integrated microfluidic applications.

Fiber In-Line Ferrofluidic Sensor

Ferrofluid is a type of stable colloidal suspension with single-domain magnetic nanoparticles that dispersed uniformly in a liquid carrier (Kruse et al. 2003). When exposed in external magnetic field, the nanoparticles inside the ferrofluid will be rearranged, resulting in change of properties of the solution such as refractive index and absorption coefficient of electromagnetic radiation (Yang et al. 2002). Based on its unique properties, a lot of magnetic field sensors have been proposed. Among them, optical fiber-based ferrofluidic sensors have attracted a lot of interests because of its compact size and high sensitivity. Various configurations of fiber-optic ferrofluid magnetic field sensors have been reported, such as singlemode-multimode-singlemode (SMS) structure (Chen et al. 2013), tapered microstructured optical fiber (Deng et al. 2015), fiber FP interferometer (Lv et al. 2014), etc.

In this section, we present a ferrofluid-based optical fiber magnetic field sensor (Fig. 22) fabricated by FLIWD technique. The glass tube (GT) was sandwiched by SMFs forming a typical FP cavity. The opening (μ-window), fabricated by FLIWD technique, offers sufficient access for the filling ferrofluid. The refractive index of the ferrofluid varies as the surrounding magnetic field strength changes, which can be optically probed by the FP interferometer. In our case, such FP interferometer is sensitive to RI change inside the cavity while insensitive to ambient temperature.

In this case, Ferrotec-Oil-based Ferrofluid EMG 909 is filled in the FP cavity. The n_{cavity} follows the equation:

$$\Delta n_{\text{cavity}} = \alpha_H \Delta H + \alpha_T \Delta T \tag{28}$$

where the Δn_{cavity} is the RI change when filling with ferrofluid liquid and α_H is the magnetic sensitivity of the ferrofluidic, while α_T is the temperature sensitivity. The thermal expansion can be ignored as the experiment environment is operated

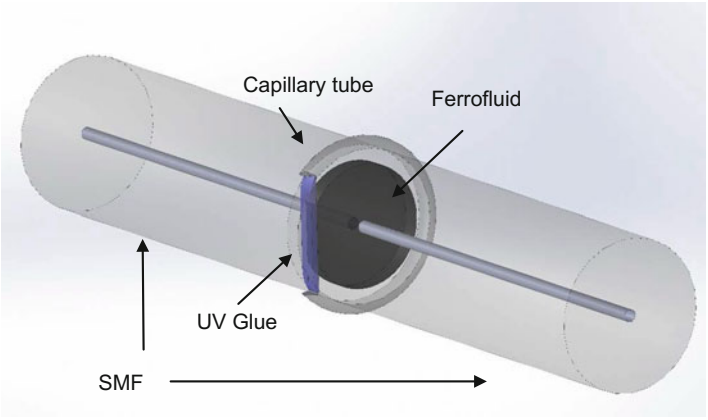

Fig. 22 The structure of sensor probe

at room temperature (21 °C). So the resonance wavelength shift of the interference spectrum is:

$$\Delta\lambda_m = \lambda_m \cdot \alpha_H \Delta H \tag{29}$$

Here we used SMF-28e (Corning) with core in 8.2 μm and cladding in 125 μm, respectively. The capillary tube used in experiment is glass tube with OD in 164 μm and ID in 100 μm. Both fiber and tube were mechanically stripped off its buffer and cleaned. First, an SMF was spliced with the capillary tube. Second, the assembly was mounted in fiber slicer and observed under measurement-controlled microscope (Nikon). The cutting point upon the capillary tube can be precisely controlled with the help of the microscope and a motorized translation stage. In order to get a highly performed FP cavity, the expected leaving length of tube is 30 μm.

To fabricate the compatible μ-window for the needle, the following steps were adopted. Figures 23 and 24 show the assembly before and after fs fabrication. The injection of ferrofluid was realized by a syringe pump and a fabricated microneedle. The approximate O.D. of the needle was around 20 μm. Then, the assembly was clamped horizontally onto two fiber holders (Newport 561-FH). The fabrication processed in water as the opening was fabricated from the surface to the deep. Then, a rectangle region with dimensions of $30 \times 60 \times 40$ μm was inscribed on the capillary tube. The fs laser irradiation swept from the top to the bottom. The total layers of sweep were 40 and then an opening appeared on the chosen region.

Assisted by the microscope and manual three-dimension stage, the needle was inserted into the cavity though the μ-window. The syringe pump used in experiment was set in 1 μl per second. The ferrofluid was EMG 909 from Ferrotic with low viscosity of 3 cP (at 27 °C) and saturation magnetization (Ms) of 220 Gauss. After the cavity was fully filled up, the μ-window was sealed by small amount of UV glue. One side of the SMF was cut to the minimum length to reduce the device breakage from bending.

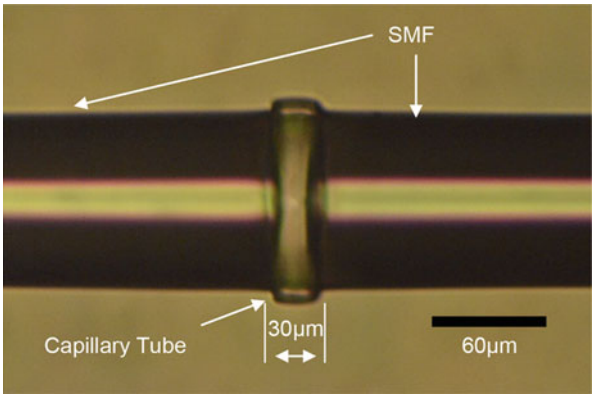

Fig. 23 The assembly before fs irradiation

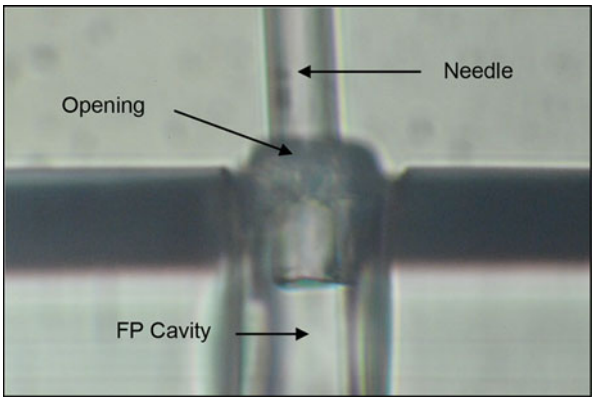

Fig. 24 The assembly after fs irradiation with needle

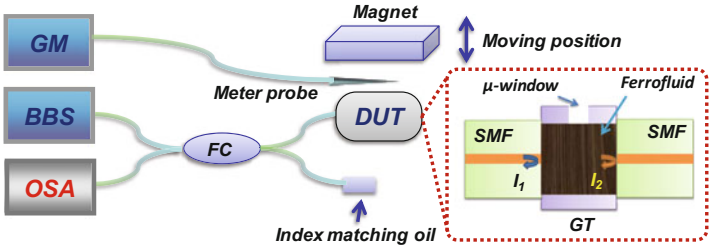

FC- Fiber coupler **DUT** - Device under test
BBS – Broad band source **GM** – Gauss meter
GT – Glass tube **SMF** – Single mode fiber

Fig. 25 The sensing system of the ferrofluidic sensor

Figure 25 shows the sensing system of the ferrofluidic sensor. The packaged device was interrogated by a broadband light source (BBS). The wavelength range is from 1520 to 1620 nm. The light was routed by a 3 dB fiber coupler (FC), and the interference spectrum was detected by an optical spectrum analyzer (OSA, AQ6319). The magnetic field is generated by a 20*20*20 mm rectangle magnet. Detector of the gauss meter was placed parallel and tightly to the sensor for precisely detecting the magnetic field intensity around. The range of magnetic field intensity applied is from 60 to 180 Gs.

The FP cavity dimension can be calculated from the FSR equation. The actual length is 31.6 μm. Figure 26 shows the interference spectrum of this ferrofluid-based magnetic field senor in magnetic field intensity at different magnetic field. As the magnetic intensity increases, the interferogram shifted toward the longer wavelength region. Figure 27 shows the spectrum valley shrift from 60 to 180 Gs with sensitivity at 0.121 nm/Gs. Linear relationship between the magnetic field intensity and the wavelength conformed the experiment principle. Similar result can be obtained with FP cavity at 50 μm as well.

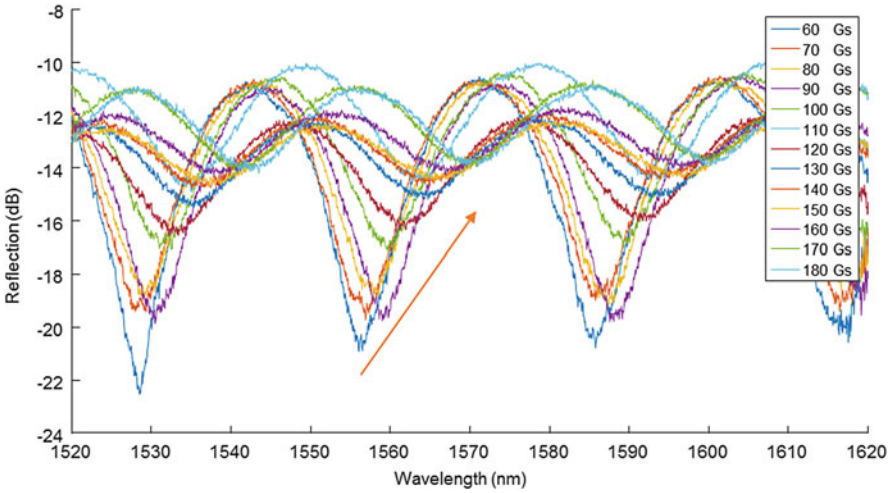

Fig. 26 The reflection spectrum of magnetic field sensor in magnetic field from 60 to 180 Gs

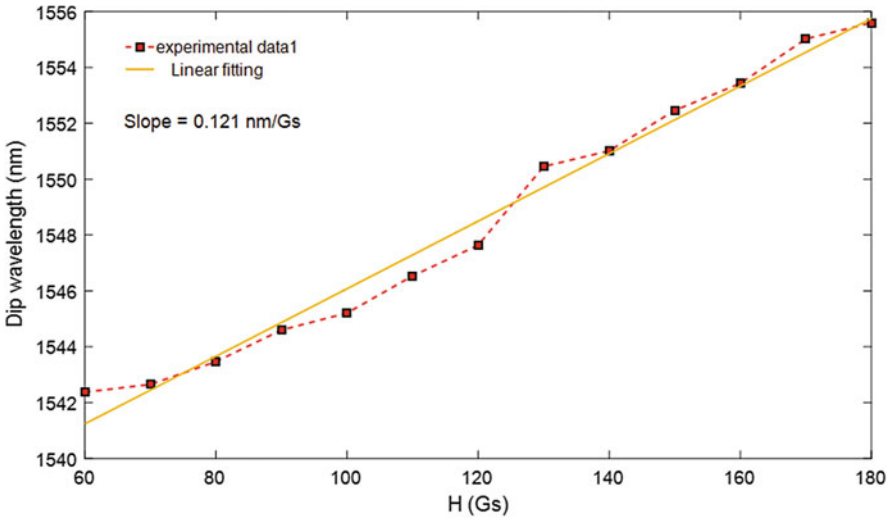

Fig. 27 Transmission spectrum at different magnetic field

In summary, a ferrofluid-based optical fiber magnetic field sensor was proposed, and the opening of the cavity was fabricated by FLIWD. The proposed sensor is novel at design and fabrication, showing impressive advantages in magnetic field sensing.

Summary

Fs laser micromachining has been proven a powerful tool for material removal and modification in transparent materials, especially in optical fibers. Due to its unique characteristic of ultrashort pulse width and extremely high peak intensity, fs laser can realize real 3D micromachining in silica or single crystal sapphire with large material bandgaps. Compared with other laser micromachining methods (i.e., UV laser, CO_2 laser, and long pulse lasers), fs laser can offer many unique advantages, such as negligible cracks, minimal heat-affected zone, low recast, high precision, and 3D structure's formation.

In this chapter, we first introduced the fundamental understanding of fs laser interaction with transparent materials for guiding the fabrication of high-performance fiber-optic sensors and devices. We then presented a typical fs laser micromachining system and the fabrication of 3D hollow structure in optical fibers with this system. As an example, an all-in-fiber 3D optofluidic microdevice was fabricated by fs laser irradiation-assisted selective chemical etching. Horizontal and vertical microchannels can be flexibly created into an optical fiber to form a fluidic cavity with inlets/outlets. The fluidic cavity also functions as an optical FP cavity in which the filled liquid can be probed. This assembly-free microdevice exhibited a high fringe visibility and demonstrated for measurement of the RI of the filling liquids. As another example, a ferrofluid-based optical fiber magnetic field sensor was fabricated by FLIWD. The structure was easy to make, and the FP cavity generated high fringe visibility. The RI changed linear theoretically with a high sensitivity of 0.121 Gs/nm.

References

R. An, Y. Li, Y. Dou, H. Yang, Q. Gong, Simultaneous multi-microhole drilling of soda-lime glass by water-assisted ablation with femtosecond laser pulses. Opt. Express **13**, 1855–1859 (2005)

R.J. Bates, *Optical Switching and Networking Handbook* (McGraw-Hill, New York, 2001)

Y. Bellouard, A. Said, M. Dugan, P. Bado, Fabrication of high-aspect ratio, micro-fluidic channels and tunnels using femtosecond laser pulses and chemical etching. Opt. Express **12**, 2120–2129 (2004)

M. Beresna, M. Gecevičius, P.G. Kazansky, Ultrafast laser direct writing and nanostructuring in transparent materials. Adv. Opt. Photon. **6**, 293–339 (2014)

V. Bhardwaj, E. Simova, P. Rajeev, C. Hnatovsky, R. Taylor, D. Rayner, P. Corkum, Optically produced arrays of planar nanostructures inside fused silica. Phys. Rev. Lett. **96**, 057404 (2006)

H.S. Carslaw, J.C. Jaeger, *Conduction of Heat in Solids*, 2nd edn. (Clarendon Press, Oxford, 1959)

Y. Chen, Q. Han, T. Liu, X. Lan, H. Xiao, Optical fiber magnetic field sensor based on single-mode-multimode-single-mode structure and magnetic fluid. Opt. Lett. **38**, 3999–4001 (2013)

B.N. Chichkov, C. Momma, S. Nolte, F. Von Alvensleben, A. Tünnermann, Femtosecond, picosecond and nanosecond laser ablation of solids. Appl. Phys. A **63**, 109–115 (1996)

A. Chimmalgi, T. Choi, C. Grigoropoulos, K. Komvopoulos, Femtosecond laser aperturless near-field nanomachining of metals assisted by scanning probe microscopy. Appl. Phys. Lett. **82**, 1146–1148 (2003)

A. Couairon, A. Mysyrowicz, Femtosecond filamentation in transparent media. Phys. Rep. **441**, 47–189 (2007)

A. Crespi, Y. Gu, B. Ngamsom, H.J. Hoekstra, C. Dongre, M. Pollnau, R. Ramponi, H.H. van den Vlekkert, P. Watts, G. Cerullo, Three-dimensional Mach-Zehnder interferometer in a microfluidic chip for spatially-resolved label-free detection. Lab. Chip **10**, 1167–1173 (2010)
K.M. Davis, K. Miura, N. Sugimoto, K. Hirao, Writing waveguides in glass with a femtosecond laser. Opt. Lett. **21**, 1729–1731 (1996)
M. Deng, C. Huang, D. Liu, W. Jin, T. Zhu, All fiber magnetic field sensor with Ferrofluid-filled tapered microstructured optical fiber interferometer. Opt. Express **23**, 20668–20674 (2015)
P. Domachuk, I. Littler, M. Cronin-Golomb, B. Eggleton, Compact resonant integrated microfluidic refractometer. Appl. Phys. Lett. **88**, 093513-1–093513-3 (2006)
D. Du, X. Liu, G. Korn, J. Squier, G. Mourou, Laser-induced breakdown by impact ionization in SiO2 with pulse widths from 7 ns to 150 fs. Appl. Phys. Lett. **64**, 3071–3073 (1994)
X. Fan, I.M. White, Optofluidic microsystems for chemical and biological analysis. Nat. Photonics **5**, 591–597 (2011)
E.G. Gamaly, S. Juodkazis, K. Nishimura, H. Misawa, B. Luther-Davies, L. Hallo, P. Nicolai, V.T. Tikhonchuk, Laser-matter interaction in the bulk of a transparent solid: confined microexplosion and void formation. Phys. Rev. B **73**, 214101 (2006)
R.R. Gattass, E. Mazur, Femtosecond laser micromachining in transparent materials. Nat. Photonics **2**, 219–225 (2008)
E.N. Glezer, E. Mazur, Ultrafast-laser driven micro-explosions in transparent materials. Appl. Phys. Lett. **71**, 882–884 (1997)
Y. Gong, Y.-J. Rao, Y. Guo, Z.-L. Ran, Y. Wu, Temperature-insensitive micro Fabry–Pérot strain sensor fabricated by chemically etching Er-doped fiber. IEEE Photon. Technol. Lett. **21**, 1725–1727 (2009)
S. Gross, M. Withford, Ultrafast-laser-inscribed 3D integrated photonics: challenges and emerging applications. Nanophotonics **4**, 332–352 (2015)
M. Haque, K.K. Lee, S. Ho, L.A. Fernandes, P.R. Herman, Chemical-assisted femtosecond laser writing of lab-in-fibers. Lab. Chip **14**, 3817–3829 (2014)
J. Hecht, *City of Light: The Story of Fiber Optics* (Oxford University Press on Demand, Oxford, 2004)
S. Ho, P.R. Herman, J.S. Aitchison, Single-and multi-scan femtosecond laser writing for selective chemical etching of cross section patternable glass micro-channels. Appl. Phys. A **106**, 5–13 (2012)
K. Itoh, W. Watanabe, S. Nolte, C.B. Schaffer, Ultrafast processes for bulk modification of transparent materials. MRS Bull. **31**, 620–625 (2006)
J.B. Jensen, L.H. Pedersen, P.E. Hoiby, L.B. Nielsen, T.P. Hansen, J.R. Folkenberg, J. Riishede, D. Noordegraaf, K. Nielsen, A. Carlsen, Photonic crystal fiber based evanescent-wave sensor for detection of biomolecules in aqueous solutions. Opt. Lett. **29**, 1974–1976 (2004)
S. Kawata, H.-B. Sun, T. Tanaka, K. Takada, Finer features for functional microdevices. Nature **412**, 697–698 (2001)
S. Kiyama, S. Matsuo, S. Hashimoto, Y. Morihira, Examination of etching agent and etching mechanism on femtosecond laser microfabrication of channels inside vitreous silica substrates. J. Phys. Chem. C **113**, 11560–11566 (2009)
T. Kruse, H.-G. Krauthäuser, A. Spanoudaki, R. Pelster, Agglomeration and chain formation in ferrofluids: two-dimensional x-ray scattering. Phys. Rev. B **67**, 094206 (2003)
S. Küper, M. Stuke, Femtosecond UV excimer laser ablation. Appl. Phys. B Lasers Opt. **44**, 199–204 (1987)
Y. Lai, K. Zhou, L. Zhang, I. Bennion, Microchannels in conventional single-mode fibers. Opt. Lett. **31**, 2559–2561 (2006)
Y. Liu, S. Qu, Y. Li, Single microchannel high-temperature fiber sensor by femtosecond laser-induced water breakdown. Opt. Lett. **38**, 335–337 (2013)
R.-Q. Lv, Y. Zhao, D. Wang, Q. Wang, Magnetic fluid-filled optical fiber Fabry–Pérot sensor for magnetic field measurement. IEEE Photon. Technol. Lett. **26**, 217–219 (2014)
T. H. Maiman, Stimulated optical radiation in ruby, 1960

S. Mao, F. Quéré, S. Guizard, X. Mao, R. Russo, G. Petite, P. Martin, Dynamics of femtosecond laser interactions with dielectrics. Appl. Phys. A Mater. Sci. Process. **79**, 1695–1709 (2004)
C. Monat, P. Domachuk, B. Eggleton, Integrated optofluidics: a new river of light. Nat. Photonics **1**, 106–114 (2007)
R. Osellame, V. Maselli, R.M. Vazquez, R. Ramponi, G. Cerullo, Integration of optical waveguides and microfluidic channels both fabricated by femtosecond laser irradiation. Appl. Phys. Lett. **90**, 231118-1–231118-3 (2007)
M.D. Perry, G. Mourou, Terawatt to petawatt subpicosecond lasers. Sci.-AAAS-Wkly. Pap. Ed.-Incl. Guide Sci. Inf. **264**, 917–923 (1994)
P. Pronko, S. Dutta, J. Squier, J. Rudd, D. Du, G. Mourou, Machining of sub-micron holes using a femtosecond laser at 800 nm. Opt. Commun. **114**, 106–110 (1995)
D. Psaltis, S.R. Quake, C. Yang, Developing optofluidic technology through the fusion of microfluidics and optics. Nature **442**, 381–386 (2006)
B. Rethfeld, A. Kaiser, M. Vicanek, G. Simon, Ultrafast dynamics of nonequilibrium electrons in metals under femtosecond laser irradiation. Phys. Rev. B **65**, 214303 (2002)
B. Rethfeld, K. Sokolowski-Tinten, D. Von Der Linde, S. Anisimov, Timescales in the response of materials to femtosecond laser excitation. Appl. Phys. A Mater. Sci. Process. **79**, 767–769 (2004)
C.B. Schaffer, A. Brodeur, E. Mazur, Laser-induced breakdown and damage in bulk transparent materials induced by tightly focused femtosecond laser pulses. Meas. Sci. Technol. **12**, 1784 (2001)
C.B. Schaffer, J.F. García, E. Mazur, Bulk heating of transparent materials using a high-repetition-rate femtosecond laser. Appl. Phys. A **76**, 351–354 (2003)
Y.-R. Shen, *The Principles of Nonlinear Optics*, vol 1 (Wiley-Interscience, New York, 1984), p. 575
D.E. Spence, P.N. Kean, W. Sibbett, 60-fsec pulse generation from a self-mode-locked Ti: sapphire laser. Opt. Lett. **16**, 42–44 (1991)
R. Stoian, D. Ashkenasi, A. Rosenfeld, E. Campbell, Coulomb explosion in ultrashort pulsed laser ablation of Al_2O_3. Phys. Rev. B **62**, 13167 (2000)
D. Strickland, G. Mourou, Compression of amplified chirped optical pulses. Opt. Commun. **55**, 447–449 (1985)
B. Stuart, M. Feit, A. Rubenchik, B. Shore, M. Perry, Laser-induced damage in dielectrics with nanosecond to subpicosecond pulses. Phys. Rev. Lett. **74**, 2248 (1995)
B.C. Stuart, M.D. Feit, S. Herman, A. Rubenchik, B. Shore, M. Perry, Nanosecond-to-femtosecond laser-induced breakdown in dielectrics. Phys. Rev. B **53**, 1749 (1996)
L. Sudrie, M. Franco, B. Prade, A. Mysyrowicz, Writing of permanent birefringent microlayers in bulk fused silica with femtosecond laser pulses. Opt. Commun. **171**, 279–284 (1999)
L. Sudrie, A. Couairon, M. Franco, B. Lamouroux, B. Prade, S. Tzortzakis, A. Mysyrowicz, Femtosecond laser-induced damage and filamentary propagation in fused silica. Phys. Rev. Lett. **89**, 186601 (2002)
C.J. Tuck, R. Hague, C. Doyle, Low cost optical fibre based Fabry–Perot strain sensor production. Meas. Sci. Technol. **17**, 2206 (2006)
E. Udd, An overview of fiber-optic sensors. Rev. Sci. Instrum. **66**, 4015–4030 (1995)
A. Wang, L. Jiang, X. Li, Y. Liu, X. Dong, L. Qu, X. Duan, Y. Lu, Mask-free patterning of high-conductivity metal nanowires in open air by spatially modulated femtosecond laser pulses. Adv. Mater. **27**, 6238–6243 (2015)
T. Wei, Y. Han, Y. Li, H.-L. Tsai, H. Xiao, Temperature-insensitive miniaturized fiber inline Fabry-Perot interferometer for highly sensitive refractive index measurement. Opt. Express **16**, 5764–5769 (2008)
A.T. Woolley, R.A. Mathies, Ultra-high-speed DNA fragment separations using microfabricated capillary array electrophoresis chips. Proc. Natl. Acad. Sci. **91**, 11348–11352 (1994)
E. Yablonovitch, N. Bloembergen, Avalanche ionization and the limiting diameter of filaments induced by light pulses in transparent media. Phys. Rev. Lett. **29**, 907 (1972)

S.Y. Yang, Y.F. Chen, H.E. Horng, C.-Y. Hong, W.S. Tse, H.C. Yang, Magnetically-modulated refractive index of magnetic fluid films. Appl. Phys. Lett. **81**, 4931 (2002)
Y. Zhang, Y. Li, T. Wei, X. Lan, Y. Huang, G. Chen, H. Xiao, Fringe visibility enhanced extrinsic Fabry–Perot interferometer using a graded index fiber collimator. IEEE Photonics J. **2**, 469–481 (2010)
Y. Zhang, L. Yuan, X. Lan, A. Kaur, J. Huang, H. Xiao, High-temperature fiber-optic Fabry–Perot interferometric pressure sensor fabricated by femtosecond laser. Opt. Lett. **38**, 4609–4612 (2013)
K. Zhou, L. Zhang, X. Chen, V. Mezentsev, I. Bennion, Microstructures made in optical fiber with femtosecond laser. Int. J. Smart Nano Mater. **1**, 237–248 (2010)
H. Zhu, I.M. White, J.D. Suter, M. Zourob, X. Fan, Opto-fluidic micro-ring resonator for sensitive label-free viral detection. Analyst **133**, 356–360 (2008)